

Searching for relativistic axions in the sky

Arpan Kar,^{a,b} Tanmoy Kumar,^c Sourov Roy,^c and Jure Zupan^d

^aCenter for Quantum Spacetime, Sogang University, Seoul 121-742, South Korea

^bDepartment of Physics, Sogang University, Seoul 121-742, South Korea

^cSchool of Physical Sciences, Indian Association for the Cultivation of Science,
2A & 2B Raja S.C. Mullick Road, Jadavpur, Kolkata 700032, India

^dDepartment of Physics, University of Cincinnati, Cincinnati, Ohio 45221, USA

E-mail: arpankarphys@gmail.com, kumartanmoy1998@gmail.com,
tps@iacs.res.in, zupanje@ucmail.uc.edu

ABSTRACT: Relativistic axions produced in decays of $\mathcal{O}(10^{-7} - 10^{-2} \text{ eV})$ dark matter (DM) partially convert to photons after traversing the galactic magnetic field, giving rise to a signal observable by the Square Kilometer Array (SKA) radio telescope. We show that for axions lighter than a few $\times 10^{-13} \text{ eV}$ a 100 h SKA observation of the local dwarf galaxy Seg I would probe parameter space not constrained by stellar cooling and cosmological observations, with sensitivity several orders of magnitude better than the planned dedicated axion dark matter search experiments. We quantify the uncertainties in the SKA sensitivity projections due to two effects that enhance the radio flux: the presence of turbulent magnetic fields inside the galaxy, and the Bose enhancement of the DM decays to axions, where the latter, in particular, warrants further study.

KEYWORDS: Axion, decaying dark matter, radio signal, SKA, turbulence, Bose enhancement

Contents

1	Introduction	1
2	Axions from decaying dark matter	3
2.1	Cosmic axion background from dark matter decays	3
2.2	Contributions from galactic DM decays	4
2.3	The effect of Bose enhancement in DM decays	5
3	Axion-photon conversion	7
3.1	Conversions in a single magnetic domain	8
3.2	Radio flux from conversions in a dwarf spheroidal galaxy	9
4	Projected SKA sensitivity	11
4.1	Details of SKA: Sensitivities and field of view	11
4.2	Projections assuming a coherent magnetic field	12
4.3	Turbulent magnetic field	14
4.4	Projected SKA reach including stimulated emission	17
5	Summary and conclusions	19
A	Iterative solutions for axion occupation number	20

1 Introduction

Pseudo-Nambu-Goldstone bosons are the low energy remnants of any spontaneously broken global symmetry, and are thus ubiquitous in beyond the Standard Model (BSM) theories. In modern parlance they are referred to as axion-like-particles (ALPs) [1–3], the terminology that we will also adopt, often shortening it to simply “axions”. It is quite possible that there is a cosmic population of axions, signaling spontaneous symmetry breaking that occurred in the early Universe [4]. These axions can be non-relativistic, constituting cold dark matter (DM) [5–7], or relativistic, giving rise to a cosmic axion background (CAB) in the form of a dark radiation [8–11].

Axions in the mass range where these are good cold DM candidates are mostly searched through their couplings to photons: for m_a below $1 \mu\text{eV}$ with lumped-circuits such as ABRACADABRA [12, 13] and DMRadio [14–16], for m_a of $1\text{--}50 \mu\text{eV}$ with haloscopes such as ADMX [17–19], HAYSTAC [20, 21] and CAST-CAPP [22], and for m_a of $50 \mu\text{eV} \text{--} 1 \text{meV}$ with a planned dielectric haloscope MADMAX [23, 24]. These experiments can also search for relativistic cosmic axions. If the axions are produced in the early universe, the bounds on ΔN_{eff} [25, 26] restrict the CAB energy density to be $\Omega_{\text{CAB}} < \Omega_{\text{CMB}}$ (for other

cosmological and astrophysical bounds see [10, 27], including bounds on axions from moduli decays [28–32], and from evaporations of primordial black holes [33]). For relativistic axions produced from late decays of DM the cosmological constraints are relaxed, and can lead to observable signals in terrestrial experiments, with ADMX (HAYSTAC) already constraining DM decay times into light axions to be several orders of magnitude longer than the age of the Universe (t_U) for DM mass m_χ in the range 5–7 μeV (above a few tens of μeV to $\sim 100 \mu\text{eV}$) [10, 34, 35].

In the present manuscript we explore the potential of the upcoming radio telescope Square Kilometre Array (SKA) [36, 37] to search for relativistic axions from DM decays, which subsequently converted to photons in the magnetic field of an astrophysical object such as the dwarf spheroidal galaxy (dSph). The wide range of frequencies ($\sim 50 \text{ MHz} - \sim 50 \text{ GHz}$) and large effective area covered by the SKA relative to existing radio telescopes [37], leads to high projected sensitivities for $m_\chi \sim 10^{-7}$ to $\sim 10^{-2}$ eV. The projected sensitivity obtained with just ~ 100 hours of observation of local dSphs is typically already well above the reach of ADMX, HAYSTAC and DMRadio. Similar studies of SKA reach, but for axion cold dark matter with $m_a \gtrsim 10^{-8}$ eV were performed in [38] using the Galactic center, in [39] using nebulae and other compact objects, in [40] using dSphs, in [41] using neutron star, the Galactic center and Galaxy cluster and in [42] using Globular cluster respectively as sources of radio signals as well as in [43] where multiple different sources were used. In contrast, the relativistic axions probed by SKA are much lighter, $m_a \lesssim 10^{-12}$ eV, when constraints on axion-photon couplings [44–46] are taken into account. The signal from 7keV DM decaying to relativistic axions that subsequently convert to photons in magnetic field of galaxy clusters, was explored in [47] as a solution for the 3.5 keV line anomaly.

In this manuscript we focus on the local ultra-faint dSph galaxy Seg I as a useful target for SKA observations, mainly due to its high mass-to-light ratio and low star formation rate [48, 49], both of which suppress the relevance of highly uncertain contributions of various astrophysical processes when estimating the SKA reach. Observations of Seg I are additionally motivated by its proximity to the Earth and its high DM content, as can be inferred from the observed mass-to-light ratio within its half-light radius. However, one can trivially adapt the analysis presented below to other galactic systems as well.

The paper is structured as follows. In section 2 we discuss the production mechanism of relativistic axions from the decays of DM inside a dSph galaxy such as Seg I, as well as from decays of extragalactic and cosmological DM distributions, paying special attention to the effect of stimulated emission. In section 3 we review the phenomenon of axions converting into photons in a regular magnetic field of a dSph. In section 4 we present the projections for the SKA sensitivity to the axion and DM parameters, with the effect of a turbulent magnetic field discussed in section 4.3, and the effect of the Bose enhancement in section 4.4. We draw our conclusions in section 5, while appendix A contains further details on the calculation of stimulated emission.

2 Axions from decaying dark matter

We assume that axions, a , are produced in the two body decays, $\chi \rightarrow aa$, where χ is a scalar DM [10, 34, 47]. If axions are much lighter than DM, $m_a \ll m_\chi$, then the $\chi \rightarrow aa$ decays result in a population of highly relativistic axions. The axion energy spectrum receives two distinct contributions: i) the Cosmic Axion Background (CAB) from extragalactic DM decays, where the contributions from different epochs in the evolution of the universe result in a continuous axion energy spectrum, and ii) from DM gravitationally bound inside various galactic structures, including dSphs, resulting in monoenergetic axions.

2.1 Cosmic axion background from dark matter decays

The differential number density of cosmic axions, $dn_a/d\omega$, produced from extragalactic DM decays throughout the evolution of the universe, is given by [10],

$$\left. \frac{dn_a}{d\omega} \right|_{\text{CAB}} = \int_{t=0}^{t_U} dt \hat{a}^3 \Gamma_\chi e^{-\Gamma_\chi t} \frac{\rho_{\text{DM}}(t)}{m_\chi} \left. \frac{dN_a}{d\omega'} \right|_{\omega'=\omega/\hat{a}}, \quad (2.1)$$

where ω is the axion energy at the present time of the Universe t_U , $\rho_{\text{DM}}(t)$ is the DM energy density at time t , and $\Gamma_\chi = 1/\tau_\chi$ is the DM decay rate. The initial axion energy spectrum at time t , $dN_a/d\omega'$, is redshifted due to the expansion of the universe, with the present day axion energy given by $\omega = \hat{a}\omega'$, where the scale factor \hat{a} is normalized such that $\hat{a}_0 = 1$ at present time.¹ In (2.1) we assumed that axions remain relativistic throughout, which is an excellent approximation for the DM and axion mass ranges we will use in the numerical analysis below.

For two-body $\chi \rightarrow aa$ decays² the initial axion spectrum is $dN_a/d\omega' = 2\delta(\omega' - m_\chi/2)$. Due to the cosmological redshift this results in a continuous present day axion spectrum with maximal energy $\omega = m_\chi/2$, i.e., the isotropic and homogeneous *cosmic axion background (CAB)*,

$$\left. \frac{dn_a}{d\omega} \right|_{\text{CAB}} = 4 \frac{\rho_{\text{DM},0}}{m_\chi^2} \frac{\exp\left(-\frac{1}{\tau_\chi} t \Big|_{\hat{a}=2\omega/m_\chi}\right)}{\tau_\chi H \Big|_{\hat{a}=2\omega/m_\chi}} \Theta(m_\chi/2 - \omega). \quad (2.2)$$

Here, Θ is the Heaviside function, $\rho_{\text{DM},0}$ the present day DM energy density, while the Hubble rate H and the time of DM decay, t , are evaluated at $\hat{a} = 2\omega/m_\chi$. Fig. 1 (top panel) shows the CAB spectra (2.2) for $m_\chi = \{1, 10, 100\} \mu\text{eV}$ and $\tau_\chi = \{10, 100\} t_U$, where $t_U \simeq 13.8$ Gyr is the age of the universe. The CAB in the energy range $\omega \sim 10^{-7} - 10^{-4}$ eV results, via axion-photon conversions in astrophysical magnetic fields, in a radio signal in a frequency range $\nu = \omega/2\pi \sim \mathcal{O}(10\text{s MHz}) - \mathcal{O}(10\text{s GHz})$, which can be probed by radio telescopes (see the discussion below). To have an observable signal in SKA we therefore require in the numerical analysis for DM mass to be in the range $m_\chi \sim 10^{-7} - 10^{-4}$ eV, see also Fig. 1 (top panel).

¹We use \hat{a} for the scale factor so that it is not confused with the axion field, a .

²We assume that $\chi \rightarrow aa$ is the dominant decay mode. The UV physics that results in a couplings to photons can also generate DM-photon couplings, and $\chi \rightarrow \gamma\gamma$ decays. While the relative size of $\chi \rightarrow aa$ and $\chi \rightarrow \gamma\gamma$ branching ratios is model dependent, typically one does have $Br(\chi \rightarrow aa) \gg Br(\chi \rightarrow \gamma\gamma)$ in large regions of parameter space (see also the discussion in [50]).

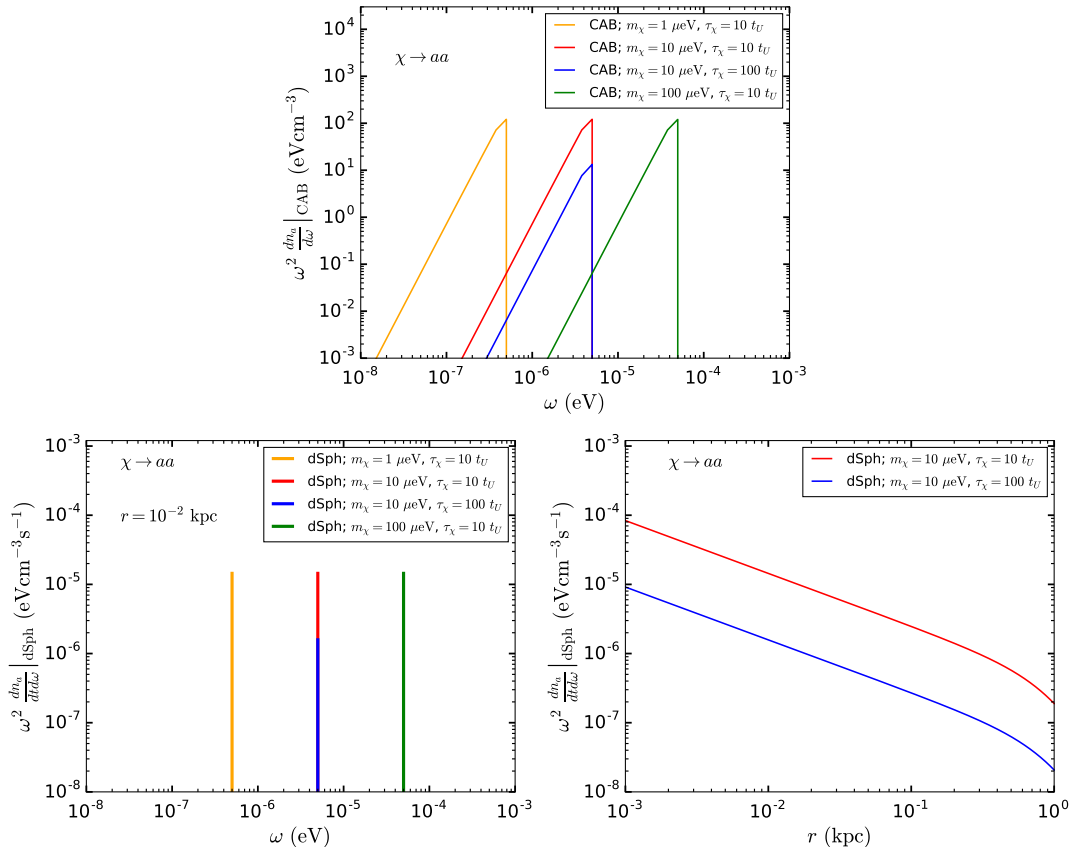


Figure 1. *Top panel:* Present day CAB spectra from extragalactic $\chi \rightarrow aa$ decays, as functions of axion energy ω , assuming the standard Λ CDM cosmological history. Color coding for each choice of DM mass, m_χ , and DM decay lifetime, τ_χ , is given in the legend. *Bottom left panel:* Differential axion flux generated from $\chi \rightarrow aa$ decays at $r = 10$ pc radial distance from the center of Seg I dSph. *Bottom right panel:* DM induced axion flux inside Seg I dSph at peak axion energy, $\omega = m_\chi/2$, cf. discussion below Eq. (2.3), as a function of the radial distance r from dSph center, for a fixed $m_\chi = 10 \mu\text{eV}$ and two values of $\tau_\chi = \{10, 100\} t_U$. All plotted spectra ignore Bose enhancements of DM decays, the effect of which is discussed in Section 2.3.

The amount of CAB sourced by the extragalactic DM decays is constrained by the observations of the CMB temperature, CMB polarization data and matter power spectra (while primordial CAB is bounded also by ΔN_{eff}). Combining Dark Energy Survey, Planck-2018, supernovae type Ia and baryonic acoustic oscillation observations, Ref. [51] finds no evidence for dark-radiation [52]. When interpreted in terms of DM decaying to dark radiation this leads to a bound $\tau_\chi \gtrsim 3.6 t_U$. In the numerical analyses below, we always choose τ_χ benchmark values such that this bound is satisfied.

2.2 Contributions from galactic DM decays

In addition to the homogeneous and isotropic CAB from decays of extragalactic DM, there is also a flux of relativistic axions from decays of galactic DM. This galactic component has directional variation. The largest axion flux originates in regions with the largest density

of DM – the galactic center and dSphs. We will be most interested in the latter, because of the reduced astrophysics backgrounds. The axion flux generated from DM decays per unit time and per unit volume of dSph galaxy is given by [10, 47],

$$\left. \frac{dn_a}{dt d\omega} \right|_{\text{dSph}}(r) = \frac{1}{m_\chi \tau_\chi} \frac{dN_a}{d\omega} \rho_{\text{DM}}^{\text{dSph}}(r), \quad (2.3)$$

where $\rho_{\text{DM}}^{\text{dSph}}(r)$ is the current DM density distribution of the dSph halo. For DM at rest, the axion energy spectrum is given by $dN_a/d\omega = 2\delta(\omega - m_\chi/2)$. For dSph DM this is spread by $\sim 10^{-5}$, which is the velocity dispersion of DM bounded inside the dSph halo, and for observations on Earth additionally by the Earth’s velocity, $\sim 10^{-3}$. Following Ref. [10], we include the two effects by taking the spectrum $dN_a/d\omega$ in Eq. (2.3) as seen by terrestrial experiments to be a Gaussian centered at $\omega = m_\chi/2$ and a width of $10^{-3}m_\chi/2$.

The energy spectrum and the spatial distribution of the axion flux from DM decays in dSph galaxy Seg I, Eq. (2.3), are shown in the two lower panels in Fig. 1. For DM distribution, $\rho_{\text{DM}}^{\text{dSph}}(r)$, we use the generalized density profile with the median values of the profile parameters in Table 4 of Ref. [53], obtained from a fit to the stellar-kinematic data.

2.3 The effect of Bose enhancement in DM decays

If the occupation number \hat{f}_a of axions in the galaxy is large, this leads to Bose enhanced stimulated DM decay rate³

$$\frac{dn_\chi}{dt} = -n_\chi \Gamma_{\text{eff}}, \quad (2.4)$$

where

$$\Gamma_{\text{eff}} = \Gamma_\chi (1 + 2\hat{f}_a), \quad (2.5)$$

is the Bose enhanced effective $\chi \rightarrow aa$ decay rate, while Γ_χ is the perturbative decay rate (for a related discussion of stimulated $a \rightarrow \gamma\gamma$ decays see [43, 54, 55]). Axion density at a radial distance r from the center of dSph is given by,

$$n_a(r) = \int d\Omega \int_{l.o.s.} ds \frac{\Gamma_{\text{eff}} N_a n_\chi}{4\pi}, \quad (2.6)$$

where N_a is the multiplicity of the final state, i.e., $N_a=2$ for $\chi \rightarrow aa$, and the integral is over solid angle and the line of sight as viewed from the position in dSph for which we calculate n_a . In the integral the DM density should be retarded. However, in practice the change in n_χ during the time it takes the axion to traverse dSph is small enough that the effect of retardation can be neglected.

The axion occupation number in the dSph halo, $\hat{f}_a(\omega)$ in Eq. (2.5), we approximate with [55]

$$\hat{f}_a(\omega = m_\chi/2) \sim \frac{n_a}{4\pi\omega^2 \Delta\omega / (2\pi)^3} = \frac{2\pi^2}{\omega^2} \frac{n_a}{\Delta\omega}. \quad (2.7)$$

Here, $\Delta\omega$ is the spread in the axion energy due to DM velocity dispersion, v_d , in dSph, $\Delta\omega = v_d(m_\chi/2)$. For Seg I dSph we take $v_d = 10$ km/s [53]. Note that the dispersion

³Since for long lived DM $n_a \ll n_\chi$ we can neglect the back-reaction due to the $aa \rightarrow \chi$ annihilations, an approximation that we expect to have only a small effect on our results.

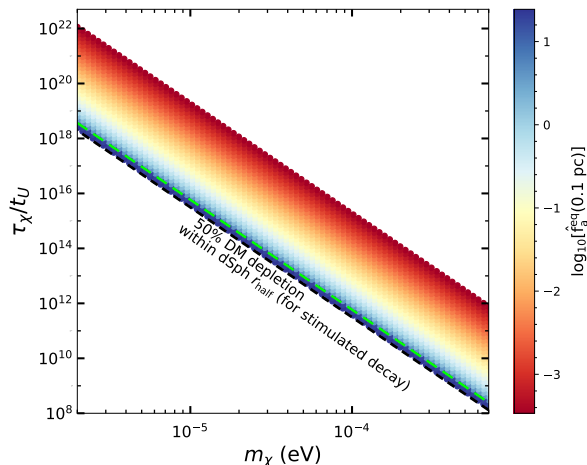


Figure 2. Occupation number \hat{f}_a (at a radius 0.1 pc inside the dSph) as a function of m_χ and τ_χ/t_U obtained by solving iteratively Eq. (2.6), see Appendix A for details. The black dashed line indicates the values of τ_χ below which our iterative procedure results in more than 50% DM depletion within the half-light radius of the dSph. Our iterative procedure is however reliable only above the green dashed line, which denotes the τ_χ values (obtained numerically) for which Δt_a (the time it takes for n_a , at 0.1 pc, to change by a factor of 2) is equal to Δt_{dSph} .

uncertainty in the axion energy is always larger than the one from the uncertainty principle $\Delta\omega\Delta t \geq 1/2$, i.e., $\Delta\omega \geq \Gamma_\chi/2$, for phenomenologically interesting perturbative decay widths, $\Gamma_\chi \ll 1/t_U$. Furthermore, the contribution from CAB to axion occupation number $\hat{f}_a(\omega = m_\chi/2)$ in dSph is negligible, and was thus not included in Eq. (2.7).

Since \hat{f}_a , and consequently Γ_{eff} , depend on n_a , cf. Eqs. (2.5) and (2.7), this means that Eq. (2.6) is an integral equation for $n_a(r)$, and as such is difficult to solve analytically. We provide instead an approximate numerical solution for the case of a slowly changing axion density, i.e., in the limit $\Delta t_a \gg \Delta t_{dSph}$. Here, Δt_{dSph} is the typical time required for a relativistic axion to traverse the dSph, $\Delta t_{dSph} \sim 1/\text{kpc} \sim 3 \cdot 10^3$ years, while Δt_a is the typical time in which n_a changes by an $\mathcal{O}(1)$ factor. Taking $\Delta n_a/\Delta t_a \simeq -dn_\chi/dt$, with $\Delta n_a \sim n_a$ gives

$$\Delta t_a \simeq \frac{\Delta n_a}{n_\chi \Gamma_\chi (1 + 2\hat{f}_a)} \sim \frac{m_\chi^4 v_d}{32\pi^2 \rho_\chi \Gamma_\chi}, \quad (2.8)$$

where in the last relation we assumed $\hat{f}_a \gg 1$, with \hat{f}_a given by (2.7) for $\omega = m_\chi/2$, and replaced $n_\chi = \rho_\chi/m_\chi$. Note that n_a drops out from the last estimate for Δt_a in (2.8) since $\hat{f}_a \propto n_a$. Numerically,

$$\Delta t_a \simeq 10^{-27} \left(\frac{m_\chi}{1 \mu\text{eV}} \right)^4 \left(\frac{v_d}{10^{-5}} \right) \left(\frac{0.1 M_\odot/\text{pc}^3}{\rho_\chi} \right) \tau_\chi. \quad (2.9)$$

Requiring $\Delta t_a \gg \Delta t_{dSph}$ then gives

$$\tau_\chi/t_U \gtrsim 10^{20} \left(1 \mu\text{eV}/m_\chi \right)^4, \quad (2.10)$$

for the parameter region where the approximation of a slowly changing axion density is valid.

In Fig. 2 we show the iterative numerical solution for $n_a(r)$ that follows from Eq. (2.6), after it is converted to the occupation number \hat{f}_a at $r = 0.1$ pc using Eq. (2.7). The iterative solution relies on the assumption of a slowly changing axion density, see details in Appendix A. It is valid above the green dashed line in Fig. 2, obtained numerically by requiring that the change from n_a to $2n_a$ takes longer than Δt_{dSph} throughout the iterative procedure. This bound coincides well with the analytical estimate, Eq. (2.10). Fig. 2 shows that in the parameter region where the iterative procedure is reliable, the effect of the stimulated emission is either negligible (for τ_χ well above the bound (2.10), in which case $\hat{f}_a \ll 1$), or only modestly important (for τ_χ close to the bound (2.10), in which case $\hat{f}_a \sim \mathcal{O}(10)$).

Extending the numerical analysis to even smaller values of τ_χ we find a runaway behavior for the n_a density so that quickly $\mathcal{O}(1)$ of DM decays within the age of the dSph (the 50% depletion is denoted with a black dashed line in Fig. 2). Since this occurs in the parameter region where our numerical approach is no longer reliable we cannot draw strong conclusions. On the one hand the observed runaway behavior could be a result of our numerical approach and the effect of stimulated emission remains modest also for smaller values of τ_χ . However, it is equally plausible that the runaway is physical, in which case the DM model we consider faces a coincidence problem – as we will see below, in this case an observable signal in SKA would require parameters close to the $\mathcal{O}(1)$ DM depletion line, raising a “why now” question?

Resolving this issue would require a more detailed numerical study, with a finely discretized description of dSph, potentially in 3D. Such a study goes beyond the scope of this paper. Instead, we show in Section 4 two sets of projections for the SKA sensitivity: first ignoring the effect of stimulated emission, and then including its effect, but limiting the analysis to the parameter region where our approximation is valid. In order to obtain the SKA reach, however, we have to first discuss the conversion of axions into photons in the galactic magnetic fields, which then leads to the observable signal in SKA.

3 Axion-photon conversion

Axions couple to photons through a dimension 5 operator [56]

$$\mathcal{L}_{a\gamma} = -\frac{1}{4}g_{a\gamma\gamma}F_{\mu\nu}\tilde{F}^{\mu\nu}a. \quad (3.1)$$

Typically, we expect $g_{a\gamma\gamma} \simeq \alpha_{\text{em}}/(4\pi f_a)$, where f_a is the axion decay constant. A value of $g_{a\gamma\gamma}$ much smaller than this naive estimate would require a fine tuned cancellation between the UV and the nonperturbative QCD contributions in the IR, which we assume not to be the case.

Due to the axion-photon interaction $\mathcal{L}_{a\gamma}$ the axion flux converts to photon flux in the magnetic field of a galaxy. We start by reviewing in Sec. 3.1 the results for axion-photon conversion in a region with homogeneous magnetic field, and then give numerical estimates for the resulting radio flux from Seg I in Sec. 3.2.

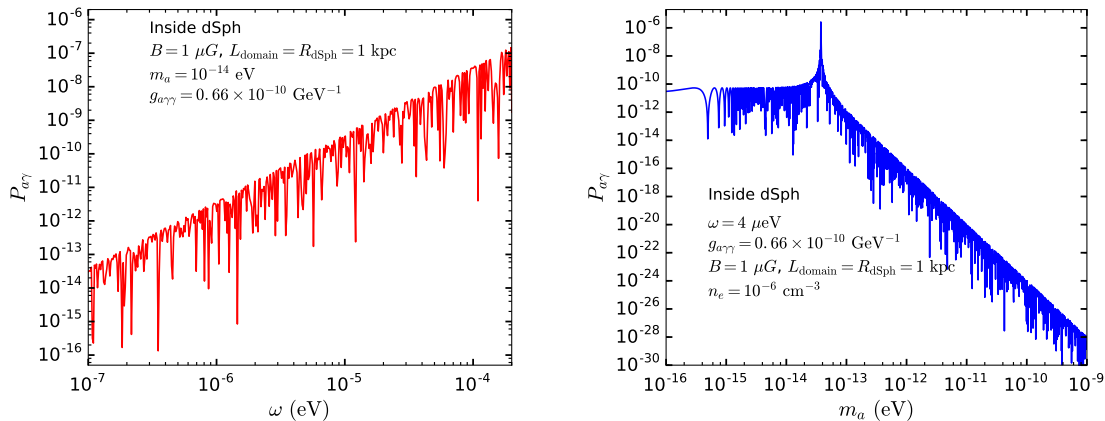


Figure 3. Axion \rightarrow photon conversion probability $P_{a\gamma}$ as a function of the axion energy ω (left panel) and axion mass m_a (right panel), for a single magnetic domain assuming a homogeneous magnetic field with a value typical for magnetic fields in a dSph (values as denoted in the legends). The sharp peak at $m_a \simeq 4 \times 10^{-14}$ eV indicates resonant conversion.

3.1 Conversions in a single magnetic domain

The probability for an axion with mass m_a and energy ω to convert to a photon, after traversing a coherent magnetic field domain of length L_{domain} , is given by [33, 57, 58],

$$P_{a\gamma} = \sin^2(2\theta) \sin^2\left(\frac{\Delta_{\text{osc}} L_{\text{domain}}}{2}\right). \quad (3.2)$$

Both the mixing angle,

$$\tan(2\theta) = \frac{2\Delta_{a\gamma}}{\Delta_{\parallel} - \Delta_a}, \quad (3.3)$$

and the oscillation frequency,

$$\Delta_{\text{osc}} = \sqrt{(\Delta_{\parallel} - \Delta_a)^2 + 4\Delta_{a\gamma}^2}, \quad (3.4)$$

depend on the product of the transverse component of the magnetic field, B_{\perp} , and the axion-photon coupling constant,

$$\Delta_{a\gamma} = \frac{1}{2} g_{a\gamma\gamma} B_{\perp} \simeq 1.52 \times 10^{-3} \text{kpc}^{-1} \times \left(\frac{g_{a\gamma\gamma}}{10^{-12} \text{GeV}^{-1}}\right) \left(\frac{B_{\perp}}{\mu\text{G}}\right), \quad (3.5)$$

where in the numerical example we chose a representative value of $g_{a\gamma\gamma}$ that can be constrained by SKA for large range of axion masses, and the value of a magnetic field typical for dSph.

The oscillation frequency corresponding to axion-photon conversions should be compared with the mismatch between the oscillations induced by the axion mass corrections

$$\Delta_a = -\frac{m_a^2}{2\omega} \simeq -7.8 \times 10^5 \left(\frac{m_a}{10^{-13} \text{eV}}\right)^2 \left(\frac{\omega}{\mu\text{eV}}\right)^{-1} \text{kpc}^{-1}, \quad (3.6)$$

and the plasma induced effects

$$\Delta_{\parallel} = \Delta_{\text{pl}} + 3.5\Delta_{\text{QED}}, \quad (3.7)$$

where

$$\Delta_{\text{pl}} = -\frac{\omega_{\text{pl}}^2}{2\omega} \simeq -1.1 \times 10^5 \left(\frac{\omega}{\mu\text{eV}}\right)^{-1} \left(\frac{n_e}{10^{-6}\text{cm}^{-3}}\right) \text{ kpc}^{-1}, \quad (3.8)$$

$$\Delta_{\text{QED}} \simeq 4.1 \times 10^{-24} \left(\frac{\omega}{\mu\text{eV}}\right) \left(\frac{B_{\perp}}{\mu\text{G}}\right)^2 \text{ kpc}^{-1}, \quad (3.9)$$

with $\omega_{\text{pl}} \simeq 3.7 \times 10^{-11} \text{eV} \times \sqrt{n_e/\text{cm}^{-3}}$ the plasma frequency, and n_e the electron density of the plasma in dSph. For $n_e \sim 10^{-6} \text{cm}^{-3}$, which is a typical value for dSphs [59, 60], the Δ_{pl} and Δ_a are of the same order for axion with a mass $m_a \sim 4 \times 10^{-14} \text{eV}$.

Fig. 3 shows the dependence of the axion→photon conversion probability $P_{a\gamma}$ inside a dSph, Eq. (3.2), on either the axion energy ω (left panel) or on the axion mass m_a (right panel). In the evaluation the magnetic field was set to $B_{\perp} = B = 1 \mu\text{G}$, a typical value for dSph galaxies such as Seg I [59–61] (in Sec. 3.2 we will also show results for a more conservative value, $B = 0.1 \mu\text{G}$). The size of the domain was taken to coincide with the dSph radius, $L_{\text{domain}} = R_{\text{dSph}} = 1 \text{kpc}$ [62], while the axion-photon coupling $g_{a\gamma\gamma} = g_{a\gamma\gamma}^{\text{SE}} = 0.66 \cdot 10^{-10} \text{GeV}^{-1}$ was chosen such that it saturates the stellar emission bounds for $m_a < 10^{-9} \text{eV}$ [10, 44]. The conversion probability $P_{a\gamma}$ shows a sharp peak at $m_a \simeq 4 \cdot 10^{-14} \text{eV}$ (cf. Fig. 3 right), for which $\Delta_{\parallel} \simeq \Delta_a$, resulting in a resonant conversion. For heavier axion masses the conversion probability rapidly decreases as $P_{a\gamma} \propto m_a^{-4}$.

3.2 Radio flux from conversions in a dwarf spheroidal galaxy

Axions that convert to photons in the magnetic field of the dSph galaxy give rise to a potentially observable signal in the radio wave frequency range. The resulting radio flux density as observed on Earth, is given by

$$S = S|_{\text{CAB}} + S|_{\text{dSph}}, \quad (3.10)$$

where $S|_{\text{CAB}}$ is the component of the flux from the CAB axions converting to photons while traversing the dSph, while $S|_{\text{dSph}}$ is due to converted axions from DM decays in the dSph itself [47].

The frequency distribution of the flux density due to CAB axions after traversing a domain of length L_{domain} that contains homogeneous magnetic field is given by [28],

$$S(\nu)|_{\text{CAB}} = \frac{P_{a\gamma}(\omega)}{L_{\text{domain}}} \times \frac{1}{4\pi\nu} \int_{\Omega} \int_{\text{l.o.s}} d\Omega ds \omega^2 \left. \frac{dn_a}{d\omega} \right|_{\text{CAB}} \quad (\text{in the units of } \text{erg cm}^{-2}\text{s}^{-1}\text{Hz}^{-1}), \quad (3.11)$$

where $\nu = \omega/2\pi$ is the frequency of the detected photon. The integration over dSph volume is in terms of a line of sight (l.o.s) coordinate s and a solid angle Ω . The CAB number density $dn_a/d\omega|_{\text{CAB}}$ is given in (2.1), while $P_{a\gamma}/L_{\text{domain}}$ is the rate per unit time at which axions convert inside a dSph [28]. Here, L_{domain} is the time it takes for an ultrarelativistic

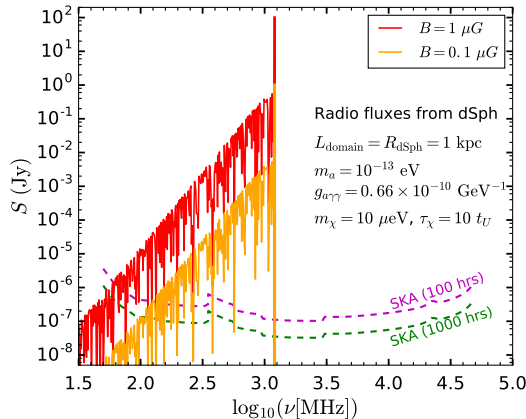


Figure 4. The red (orange) line shows the radio flux density from Seg I dSph from conversion of relativistic axions (produced in $\chi \rightarrow aa$ decays), assuming $B = 1\mu G$ ($0.1\mu G$) homogeneous magnetic field inside Seg I (the other parameters are as listed in the legend, and we ignore the effect of stimulated emission). The broad continuum is due to the CAB, while the monochromatic line at the high frequency cut-off is from the DM decays in the dSph halo. The magenta (green) dashed line shows the projected SKA sensitivity for 100 (1000) hours of observations.

axion to traverse the dSph, while the conversion probability $P_{a\gamma}$ is given by Eqs. (3.2)–(3.9). The total flux density on Earth is then obtained by summing different contributions along the line of sight.

Similarly, the radio flux density from axions that were emitted in DM decays within dSph halo and then convert to photons in the domain of length L_{domain} is given by [40, 47],

$$S(\nu)|_{\text{dSph}} = P_{a\gamma}(\omega) \times \frac{1}{4\pi\nu} \int_{\Omega} \int_{\text{l.o.s}} d\Omega ds \omega^2 \left. \frac{dn_a}{dt d\omega} \right|_{\text{dSph}} \quad (\text{in the units of } \text{erg cm}^{-2} \text{s}^{-1} \text{Hz}^{-1}), \quad (3.12)$$

where $dn_a/dt d\omega|_{\text{dSph}}$ is given in Eq. (2.3), and $P_{a\gamma}$ by Eqs. (3.2)–(3.9). As for CAB component, the total flux density observed on Earth is given by summing different contributions along the line of sight. For SKA projections in Section 4 we will consider two cases: that dSph has a completely coherent magnetic field, as well as the possibility that the magnetic field has a turbulent component. In the numerical estimates of the flux density S we use the conventional units of Jy, where $1 \text{ Jy} = 10^{-23} \text{ erg cm}^{-2} \text{ s}^{-1} \text{ Hz}^{-1}$.

Before moving to the SKA projections, it is insightful to calculate the axion conversion radio flux density S that can be expected from the ultra-faint dSph Seg I. As a representative example we take $m_\chi = 10 \mu\text{eV}$, $\tau_\chi = 10 t_U$, $m_a = 10^{-13} \text{ eV}$ and $g_{a\gamma\gamma} = 0.66 \times 10^{-10} \text{ GeV}^{-1}$, and consider the case of a homogeneous magnetic field $B = 1(0.1) \mu\text{G}$ inside the dSph, i.e., we take $L_{\text{domain}} = R_{\text{dSph}} = 1 \text{ kpc}$, and $n_e = 10^{-6} \text{ cm}^{-3}$ (in line with Refs. [60–63]), and use the same DM profile for Seg I as in Section 2.2. The predicted flux density is shown with red (orange) line in Fig. 4. It consists of a sharp monochromatic line at $\nu = (m_\chi/2)(1/2\pi)$, due to the DM decays inside dSph, and a tail at lower frequencies, due to conversions of CAB axions. The flux density due to DM decays in the dSph gives the dominant contribution to the integrated radio flux density, a consequence of a much

higher DM density in the dSph halo. Note that the expected radio flux density drops with decreased magnetic field, in line with the expected decrease in the conversion probability, cf. Eq. (3.2). Fig. 4 also shows the expected sensitivities of the SKA radio telescope after 100 (magenta dashed line) and 1000 hours of observations (green dashed line). Further details about these projections are given in the next section.

4 Projected SKA sensitivity

Next, we discuss the SKA sensitivity to axion parameters, m_a , $g_{a\gamma\gamma}$, and DM parameters, m_χ, τ_χ , assuming that SKA would observe Seg I for either 100 or 1000 hours.

4.1 Details of SKA: Sensitivities and field of view

The Square Kilometer Array (SKA) is a next generation radio telescope array currently under construction. The SKA is expected to operate in a wide frequency spectrum stretching from roughly few tens of MHz to few tens of GHz. The SKA will also make use of various technologies to expand its field of view (FOV), thereby enabling it to instantaneously image a large portion of the sky [64–66]. The SKA will also allow us to digitally patch multiple FOVs to observe a wide region of interest in the sky [67]. Similar technique of patching multiple FOVs to image a large portion of the sky at a time is also used by other telescopes like the Jansky Very Large Array [68, 69]. These techniques, in turn, will enable the SKA array to attain an effective FOV ranging from 200 square degrees to 1 square degree, depending on the frequency of observation [64]. Thus apart from a small portion in the high frequency end of the spectrum, in the majority of the radio frequency spectrum, the entire emission region of dSph like Seg I can be visible within the effective FOV of the SKA array. Consequently, for simplicity, we consider that almost all the radio flux originating from the entire dSph emission region can be captured by SKA and will contribute to the detected signal.

Furthermore, the SKA is also projected to be the most sensitive radio telescope till date. Since the telescope is yet to start operations, exact values of the rms surface brightness sensitivity of the SKA array across the frequency range, in the direction of the dSph, are not yet available. Using the presently accepted SKA baseline design, ref. [37] has provided an averaged ($T_{\text{sys}}/A_{\text{eff}}$) for SKA-Low and SKA-Mid arrays, which is averaged over all solid angles within 45 degrees of the zenith, as a function of the observing frequency. Here A_{eff} is the effective collecting area of the array and T_{sys} is the system temperature. For this work, in order to present our bounds on the axion and DM parameter spaces, we have considered this averaged ($T_{\text{sys}}/A_{\text{eff}}$) to estimate the SKA sensitivity. The expected rms surface brightness sensitivity or equivalently the rms noise level of both the SKA-Low and SKA-Mid arrays, N_{rms} , are then obtained as [40, 70]

$$N_{\text{rms}} = 2 \frac{T_{\text{sys}}}{A_{\text{eff}} \sqrt{\Delta\nu t_{\text{obs}}}} \quad (4.1)$$

where $\Delta\nu$ is the instantaneous bandwidth and t_{obs} is the observation time. For calculating the instantaneous bandwidth $\Delta\nu$ we follow the presently accepted baseline design [37].

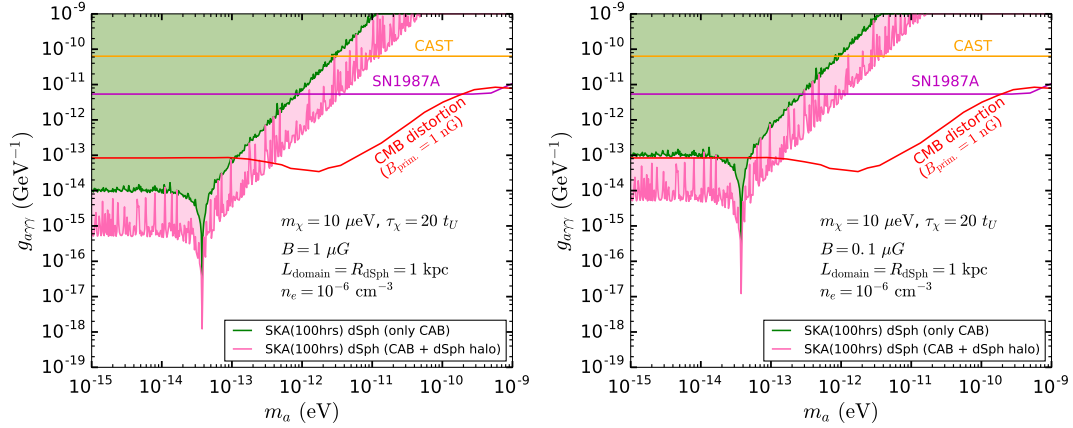


Figure 5. Regions in pink show the projected SKA reach in the $m_a - g_{a\gamma\gamma}$ plane, assuming either $B = 1 \mu\text{G}$ regular magnetic field (left panel) or $B = 0.1 \mu\text{G}$ (right panel), and 100 hours of observation time in the direction of dSph Seg I (green region shows the reach from the CAB contribution to the radio flux). The DM and astrophysical parameters are as listed in the panels. Solid lines indicate present upper-limits on $g_{a\gamma\gamma}$ from CAST (orange), SN 1987A (magenta) and CMB distortions (red).

The expected rms surface brightness sensitivity for two values of t_{obs} - 100 hours and 1000 hours - are shown in Fig. 4 by the dashed magenta and green lines respectively. To simplify our calculation we assume that the array sensitivity of SKA for an enlarged FOV is the same as those shown in Fig. 4. In order to get a more accurate sensitivity, a detailed calculation is required that will depend on the actual configuration of the SKA when it is fully operational, which at present is beyond the scope of this work.

We then define the SKA projected reach as in [71]: the radio signal is deemed to be detectable if it is 3 times larger than the rms noise level (N_{rms}) in at least one frequency bin in the SKA frequency range, ~ 50 MHz to ~ 50 GHz [37].

The projections have two main uncertainties: the knowledge of the magnetic field in Seg I, and whether or not the stimulated axion emission is an important effect. To assess the first uncertainty we consider several values of the magnetic field, to start with assuming in Section 4.2 that the magnetic field is to a good approximation homogeneous, and then including the effect of a turbulent component in Section 4.3, in both cases ignoring stimulated emissions. The projections for the parameter region for which our calculation of stimulated emission is valid are discussed in Section 4.4.

4.2 Projections assuming a coherent magnetic field

Figs. 5 and 6 show in pink the projected SKA reach in the $m_a - g_{a\gamma\gamma}$ and $m_\chi - \tau_\chi$ plane, respectively, assuming that the magnetic field in Seg I is homogeneous, with its flux density equal to either $B = 1 \mu\text{G}$ (left panels, a more typical value) or $B = 0.1 \mu\text{G}$ (right panels, a conservative value). We use the same values of $L_{\text{domain}} = R_{\text{dSph}} = 1$ kpc and $n_e = 10^{-6} \text{cm}^{-3}$ as in Fig. 3. The green shaded regions in Figs. 5 and 6 indicate the SKA reach that would be obtained from the subdominant CAB contribution to the radio flux.

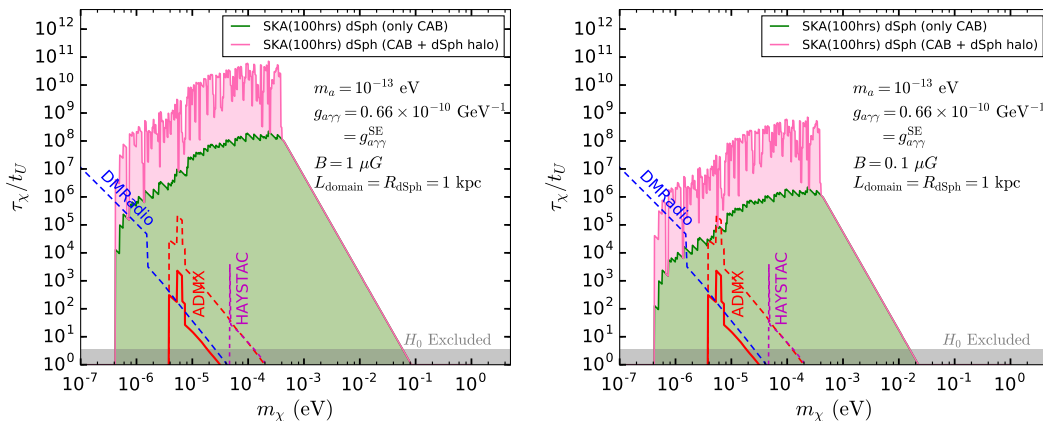


Figure 6. Same as Fig. 5, but for the projected 100h SKA reach in the DM parameter space. The solid red line denotes the present bound (lower-limit) from the ADMX experiment, while dashed lines give future sensitivities of ADMX (red), HAYSTAC (magenta) and DMRadio (blue). The gray shaded region is excluded by H_0 measurements, see main text for further details.

In the example in Fig. 5 we set DM lifetime to $\tau_\chi = 20 t_U$ and DM mass to $m_\chi = 10\mu\text{eV}$. For larger DM lifetimes the reach in $g_{a\gamma\gamma}$ drops as $\sim 1/\sqrt{\tau_\chi}$, while for heavier DM masses the region of SKA sensitivity moves to higher m_a . The sharp increase in the SKA sensitivity at $m_a \simeq 4 \times 10^{-14}\text{eV}$ is the result of a resonant conversion, where the resonant m_a depends on the assumed value of electron number density as $\sim \sqrt{n_e}$, see Section 3.1. For $m_a \gtrsim \text{few} \times 10^{-13}\text{eV}$ the SKA sensitivity falls rapidly with the increasing m_a , following the corresponding drop in the axion-photon conversion probability, c.f. Fig. 3. For $m_a \lesssim \text{few} \times 10^{-13}\text{eV}$, on the other hand, the projected SKA reach is well beyond the present bounds on axion couplings to photons: the present bound from CAST helioscope search for solar axions (orange line) [44], the bound due to non-observation of gamma-rays from conversions of SN 1987A emitted axions (magenta) [45], and from bounds on CMB distortions that would be caused by conversion of CMB photons into axions (red) [46]. Note that the CMB distortions depend strongly on the value of the primordial magnetic flux density. For the exclusion line in Fig. 5 we assume $B_{\text{prim.}} = 1\text{ nG}$, comparable to the current upper limits from CMB measurements [72].

Fig. 6 shows the projected SKA reach in the $m_\chi - \tau_\chi$ plane, setting the axion parameters to $m_a = 10^{-13}\text{eV}$ and $g_{a\gamma\gamma} = 0.66 \times 10^{-10}\text{GeV}^{-1}$, and the same color coding as in Fig. 5. For smaller values of $g_{a\gamma\gamma}$ the reach in τ_χ drops as $1/g_{a\gamma\gamma}^2$. For heavier m_a the parameter region probed by SKA would move to higher values of DM mass, with a diminishing reach, while for smaller m_a the reach can be even much higher, cf. Fig. 5. The DM mass range probed also depends on the value of the B -field in the target dSph: for the examples shown in Fig. 6, SKA will probe a DM mass in the range $4 \times 10^{-7}\text{eV}$ to $\sim 10^{-1}\text{eV}$ (left panel) or to $\sim 10^{-2}\text{eV}$ (right panel). Note that for axion parameters used in Fig. 6, DM lighter than $4 \times 10^{-7}\text{eV}$ results in a conversion photon signal below the observable frequency range of the SKA, resulting in a sharp drop in the SKA sensitivity at low DM masses. At the upper end of the probed DM mass range, the monochromatic part of the signal is

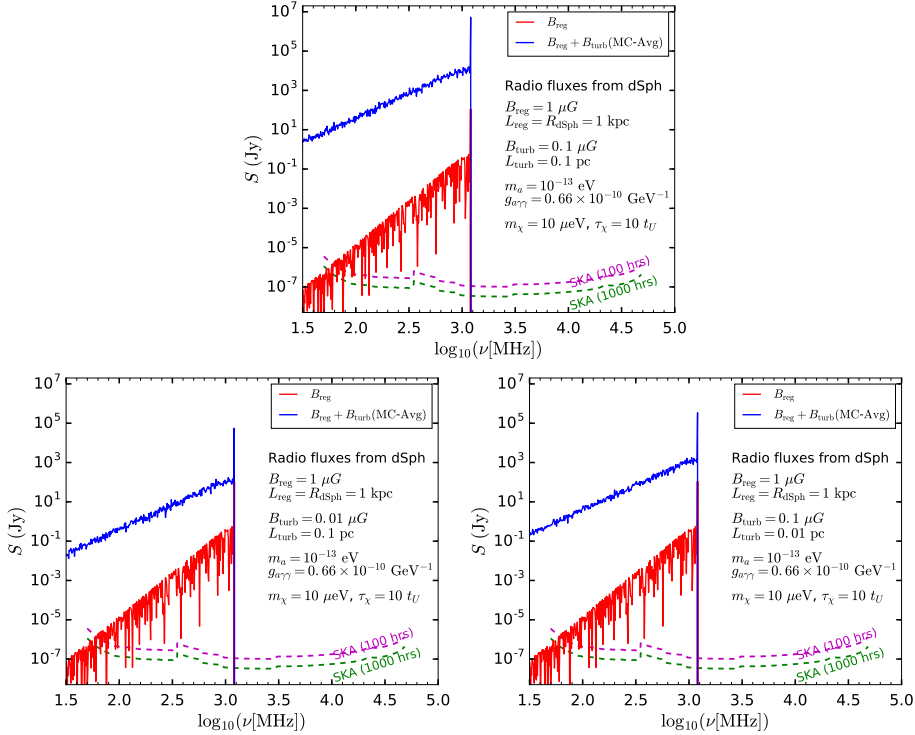


Figure 7. The radio flux density S from $\chi \rightarrow aa$ axions converted to photons in the magnetic field of Seg I, either assuming regular magnetic field (red curve) or in addition the turbulent component with the parameters listed in Eq. (4.2): (a) – top panel, (b) – bottom left, (c) – bottom right. The SKA sensitivity for 100 (1000) hours of observation is shown with magenta (green) dashed line. The axion and DM parameters are as listed in the panels.

outside the SKA frequency range, and thus the signal in SKA is entirely due to the CAB contribution, leading to a slow drop in sensitivity for higher masses due to the falling axion flux (this is proportional to the average DM number density and thus $\propto 1/m_\chi$). Note that the SKA reach in the relevant DM mass range is well above the present exclusions: from the H_0 measurements (gray shaded area) [51], from ADMX (solid red line) [10], as well as future sensitivities from ADMX (dashed red), HAYSTAC (dashed magenta) and DMRadio (dashed blue), see Ref. [10] for further details on these projections.

4.3 Turbulent magnetic field

So far we assumed that dSphs have only regular magnetic field with coherence length $\sim 1 \text{ kpc}$. Galaxies, including dSphs, can also host a turbulent magnetic field component with small coherence length, L_{turb} , and root mean square (rms) amplitude, B_{turb} [40, 58, 63, 73, 74]. As we show below, the addition of such a small scale turbulent magnetic field increases the axion \rightarrow photon conversion probability $P_{a\gamma}$ [58], and consequently increases the SKA reach.

In galaxies such as Milky Way and M31, B_{turb} is typically of the same order as the strength of the regular field, B_{reg} , while L_{turb} is two to three orders of magnitude smaller

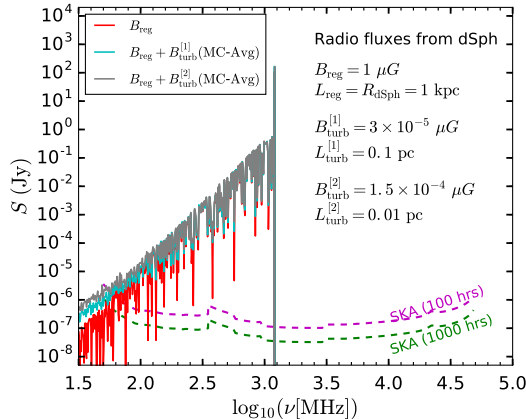


Figure 8. For small enough turbulent magnetic fields, e.g., $B_{\text{turb}} = 3 \times 10^{-5} \mu\text{G}$ for $L_{\text{turb}} = 0.1 \text{ pc}$ (cyan) and $B_{\text{turb}} = 1.5 \times 10^{-4} \mu\text{G}$ for $L_{\text{turb}} = 0.01 \text{ pc}$ (gray) the radio flux density S is indistinguishable from the case of a regular magnetic field (red). The values of axion, DM, and regular magnetic field parameters, as well as the color coding for SKA sensitivities, are as in Fig. 7.

than the coherence length of the regular field, L_{reg} [58, 75]. For dSphs the values of B_{turb} and L_{turb} , on the other hand, are highly uncertain. For Seg I we explore three representative cases,

$$(a) \quad B_{\text{turb}} = 0.1 \mu\text{G}, \quad L_{\text{turb}} = 0.1 \text{ pc}, \quad (4.2a)$$

$$(b) \quad B_{\text{turb}} = 0.01 \mu\text{G}, \quad L_{\text{turb}} = 0.1 \text{ pc}, \quad (4.2b)$$

$$(c) \quad B_{\text{turb}} = 0.1 \mu\text{G}, \quad L_{\text{turb}} = 0.01 \text{ pc}, \quad (4.2c)$$

For regular magnetic field we take, as in Section 4.2, $B_{\text{reg}} = 1 \mu\text{G}$ and $L_{\text{reg}} = R_{\text{dSph}} = 1 \text{ kpc}$.

Fig. 7 shows the predicted radio flux density from axion conversions in Seg I, either assuming just the regular magnetic field component (red lines) or in addition also the turbulent magnetic field component (blue lines), for the three representative cases in (4.2). The radio flux density in the case of a turbulent magnetic field was obtained from the “cell-model” of Ref. [58], with the cell size set to $L_{\text{cell}} = 2L_{\text{turb}}$. For each parameter set in (4.2) we performed a Monte Carlo (MC) simulation with 10 realizations of the turbulent field, divided into cells, calculated axion \rightarrow photon conversion probability $P_{a\gamma}$, and then averaged it over the 10 realizations. In calculating the radio flux density both CAB and the dSph halo contributions were included, with the axion and DM parameters set to $m_a = 10^{-13} \text{ eV}$, $g_{a\gamma\gamma} = 0.66 \times 10^{-10} \text{ GeV}^{-1}$, $m_\chi = 10 \mu\text{eV}$, $\tau_\chi = 10t_U$.

The enhancement of the radio flux density S due to the turbulent magnetic field is several orders of magnitudes. It depends on both B_{turb} and L_{turb} , where for chosen parameters S increases if either B_{turb} or L_{turb} increase, see Fig. 7. For small enough B_{turb} the axion-photon conversion probability becomes indistinguishable from having just the regular magnetic field, see the examples in Fig. 8. The threshold value of B_{turb} , below which the effect of turbulent magnetic field is negligible, depends on the value of L_{turb} , and is for instance $B_{\text{turb}} \simeq 3 \times 10^{-5} \mu\text{G}$ for $L_{\text{turb}} = 0.1 \text{ pc}$ (cyan line), and $B_{\text{turb}} \simeq 1.5 \times 10^{-4} \mu\text{G}$ for $L_{\text{turb}} = 0.01 \text{ pc}$ (grey), see Fig. 8, for the axion and DM parameter as in Fig. 7. The

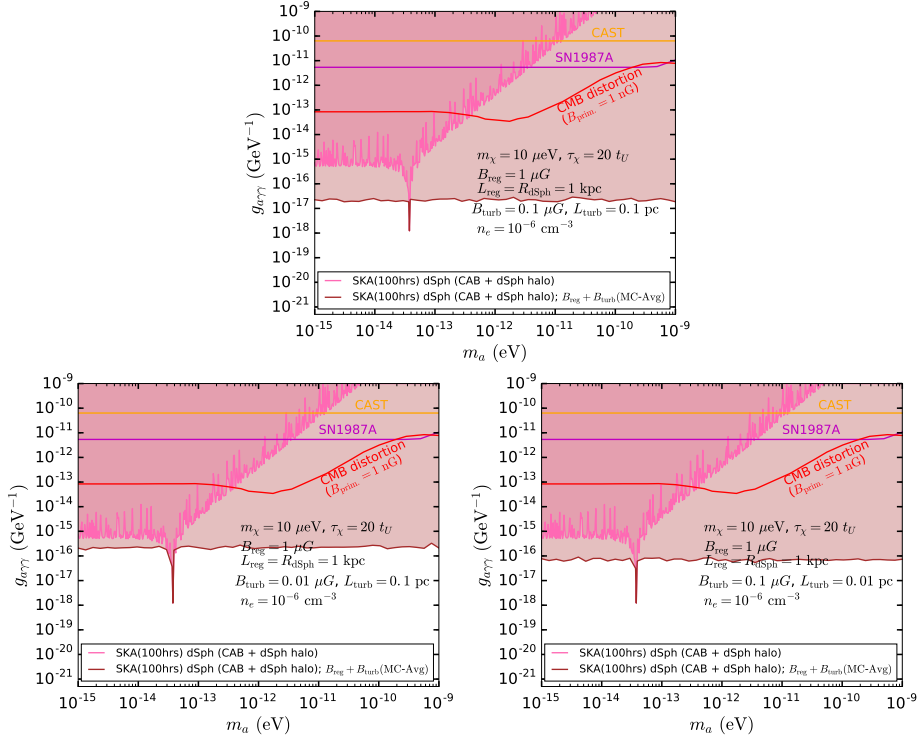


Figure 9. The expected SKA sensitivity reach in the $m_a - g_{a\gamma\gamma}$ plane after 100 hours of Seg I observations, for either just the regular magnetic field (pink) or for, in addition, the turbulent component (brown) from Eq. (4.2): (a) – top panel, (b) – bottom left, (c) – bottom right. The DM and the regular magnetic field parameters are as in Fig. 7. The orange, magenta and red solid lines denote the existing bounds from CAST, SN 1987A and CMB distortions, respectively.

threshold value of B_{turb} also depends on m_a and m_χ . For example, for $m_a > 10^{-13}$ eV, the threshold value of B_{turb} is smaller than in the two examples. In all cases we checked that the threshold values of B_{turb} we obtain here are well below the value of B_{turb} expected in local dSphs such as Seg I, if one assumes similar scaling between B_{reg} and B_{turb} as is usually assumed for Milky Way. The projected SKA sensitivities obtained in Section 4.2 can thus be viewed as fairly conservative (note though that these still neglect stimulated emission).

The effect of the turbulent magnetic field component on the SKA reach is clearly visible in Figs. 9 and 10. These show the projected SKA reach (brown) in the $g_{a\gamma\gamma} - m_a$ and $m_\chi - \tau_\chi$ planes, respectively, after 100 hours of Seg I observation, for the three representative turbulent magnetic field parameter sets in Eq. (4.2), to be compared with the corresponding SKA reach assuming just the regular magnetic field (pink). All the parameters that are not varied, including the regular magnetic field parameters, are as in Fig. 7. The presence of a turbulent magnetic field component improves significantly the projected SKA sensitivities on $g_{a\gamma\gamma}$, especially for axion masses above 10^{-13} eV, see Fig. 9. Similarly, if there is a turbulent magnetic field component in Seg I, this will increase the SKA sensitivity to DM decay time, especially for m_χ in the range $4 \times 10^{-7} \sim 2 \times 10^{-4}$ eV, see Fig. 10.

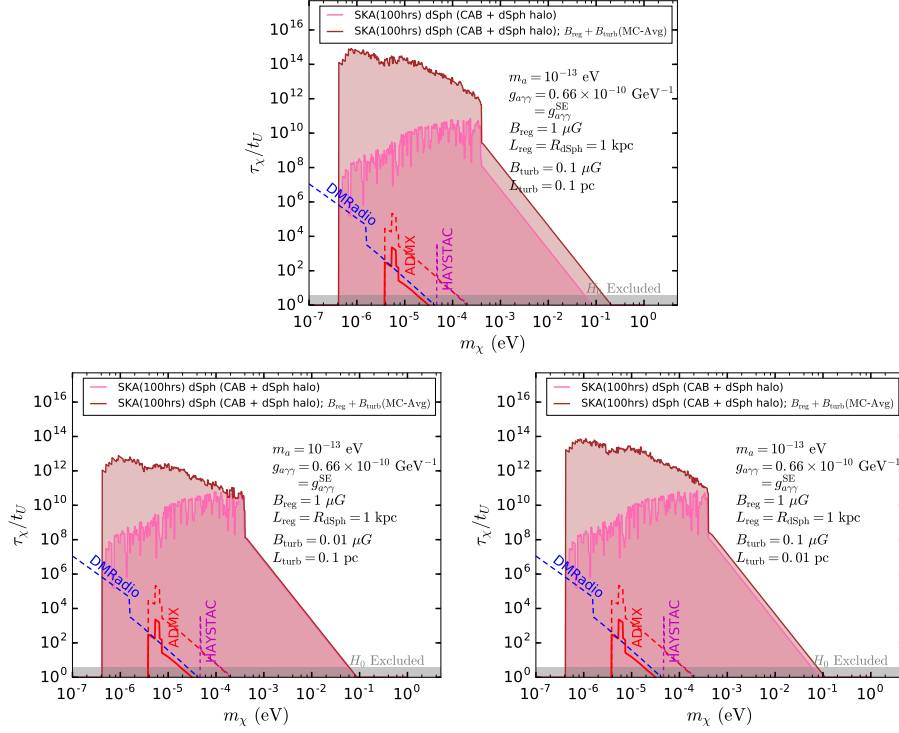


Figure 10. The projected SKA reach in the $m_\chi - \tau_\chi$ plane after 100 hours of Seg I observations with the turbulent magnetic field parameters and color coding as in Fig. 9, while the axion and the regular magnetic field parameters are as in Fig. 7. The color coding for the other exclusions is as in Fig. 6.

4.4 Projected SKA reach including stimulated emission

Finally, let us turn to the predictions of SKA reach that includes the effect of stimulated emissions. The radio flux density due to converted axions is then given by Eq. (3.12), after replacing the DM decay time in the expression for $dn_a/dtd\omega|_{\text{dSph}}$, Eq. (2.3), with the effective decay time, $\tau_\chi \rightarrow 1/\Gamma_{\text{eff}}$. The radio flux density is then given by

$$S(\nu) = P_{a\gamma}(\omega) \times \frac{1}{4\pi\nu} \int_{\Omega} \int_{\text{l.o.s}} d\Omega ds \omega^2 \Gamma_{\text{eff}}(s) \frac{dN_a}{d\omega} n_\chi \quad (\text{in the units of } \text{erg cm}^{-2} \text{s}^{-1} \text{Hz}^{-1}), \quad (4.3)$$

where the energy spread in the photon signal, encoded in $dN_a/d\omega$, is due to both the dSph DM velocity spread as well as due to the velocity of the Earth, and is modeled via Gaussian smearing as in Section 2.2. Here $\nu = \omega/2\pi$ is the frequency of the detected photon. For simplicity, we only consider the case of a homogeneous magnetic field in the dSph, so that the axion \rightarrow photon conversion probability $P_{a\gamma}(\omega)$ is given by the expressions in Section 3.1, taking dSph as a single magnetic domain (cf. also the analysis in Section 4.2). Just like before (cf. also the analysis in Section 3.2), in the numerical estimates of the flux density S we use the conventional units of Jy, where $1 \text{ Jy} = 10^{-23} \text{ erg cm}^{-2} \text{ s}^{-1} \text{ Hz}^{-1}$.

Note that the effective decay width in (4.3) is position dependent, since it depends on the local axion density, n_a , see (2.5). It is calculated in the limit of slowly varying axion

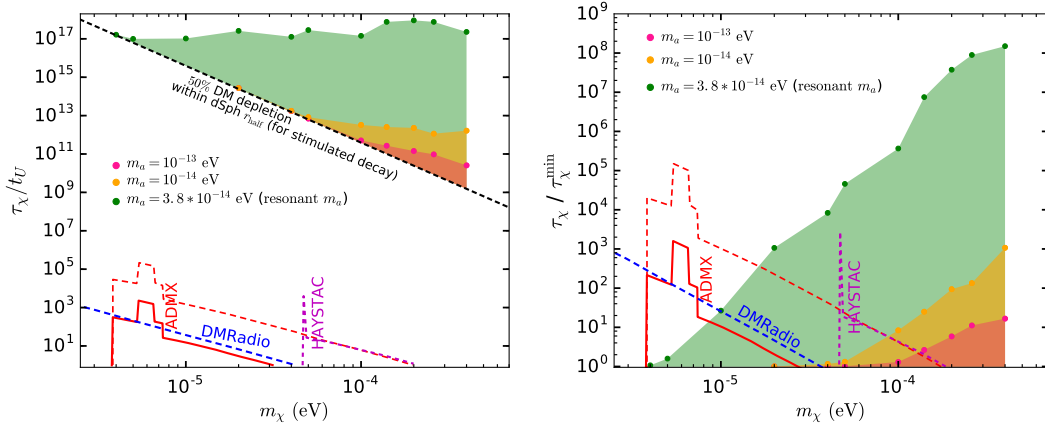


Figure 11. The 100h SKA reach in τ_χ/t_U (left) and $\tau_\chi/\tau_\chi^{\min}$ (right) for three axion masses, $m_a = \{1, 3.8, 10\} \times 10^{-14}$ eV ($\{\text{orange, green, pink}\}$), using only the dominant contribution to the radio flux density, i.e., from DM decays in dSph. The other axion and astrophysical parameters, as well as the (projected) exclusions from other experiments, are the same as those used in the left panel of Fig. 6. The parameter region above the dashed black line in the left panel corresponds to slow enough DM decays, see discussion in the main text.

density using the iterative procedure detailed in Section 2.3 and in Appendix A. Using this procedure also outside its region of validity one finds a runaway behavior. If this is a physical effect most of the axion and DM parameter region that can be probed by SKA (and other experiments) is already excluded, since it results in DM decaying too quickly. This can be seen from Fig. 11 (left) where we show the 100h SKA reach in the $m_\chi - \tau_\chi$ plane for three axion masses: $m_a = 3.8 \times 10^{-14}$ eV (green) that leads to resonant conversion and thus the highest SKA reach, and two axion masses, below and above the resonant conversion, $m_a = 10^{-14}$ eV (pink) and $m_a = 10^{-13}$ eV (orange), respectively. Other axion and astrophysical parameters are the same as those used in the left panel of Fig. 6. The same is true for the plotted exclusion lines from the other experiments, i.e., they are as in Fig. 6 and in particular ignore the effects of stimulated emissions. In calculating the SKA reach we considered for numerical expedience only the contribution from the decay of local DM particles in the dSph halo, i.e., we neglected the CAB contribution, which explains the sharp cut-off of SKA sensitivity at high DM masses (cf. Fig. 6). In fact, since estimating Γ_{eff} is rather numerically intensive, the SKA reach calculation shown in Fig. 11 is rather coarse grained, with dots denoting the calculated values, and the remainder obtained through linear interpolation to guide the eye.

The dashed black line in Fig. 11 (left) denotes the maximum allowed value of Γ_χ (minimal allowed value of τ_χ), which we define to be the Γ_χ for which 50% of DM contained within half-light radius of the dSph decays during the evolution of dSph until the present time (this corresponds to roughly $\sim 10\%$ depletion of total dSph DM mass). From numerical analysis we obtain,

$$\Gamma_\chi^{\max}(m_\chi) \equiv 1/\tau_\chi^{\min} \simeq 5.86 \times 10^{-38} \times \left(\frac{m_\chi}{1 \mu\text{eV}} \right)^4 s^{-1}. \quad (4.4)$$

Note that while this line is in the region outside the validity of our iterative procedure, it is not very far away from it (cf. Fig. 2). For reader’s convenience we also show the projected 100h SKA reach in terms of normalized DM decay time, $\tau_\chi/\tau_\chi^{\min}$, in Fig. 11 (right). We see that a discovery of axion by the SKA would require a coincidence, a DM that has just the right decay time that it does not lead to too quick DM decays, but still small enough that it gives an observable radio signal. The other option is that the axion mass is such that resonant conversion is possible. Two comments are in order, though. First of all, as already discussed in Section 2.3, establishing whether shorter DM decay times really do lead to a physical runaway behavior would require a more detailed numerical simulation that takes into account the possibility of a rapidly changing axion field. Secondly, even if the runaway behavior is physical, improving the SKA reach (either by an increased exposure time or relying on spectral features) would drive the observations away from the “just-now” parameter region.

5 Summary and conclusions

In this manuscript we explored a rather simple modification of the minimal DM scenario, allowing for DM to be accompanied by a light pseudoscalar, an axion a , such that DM is unstable and decays through the $\chi \rightarrow aa$ channel (for simplicity we assume DM to be a scalar). This is still a rather generic possibility given that a dark sector with a spontaneously broken global symmetry will result in a pNGB, i.e., such a light pseudoscalar.

We were most interested in the possibility that axion couples to photons, in which case it can be searched for in terrestrial experiments. DM decays produce relativistic axions, which then convert to photons in the magnetic field of a galaxy such as a dSph. As we showed in the paper, this process can lead to a detectable signal in the upcoming SKA radio telescope for DM masses in the range $\text{few} \times 10^{-7} \text{ eV} < m_\chi < \text{few} \times 10^{-2} \text{ eV}$. Assuming a 100 h SKA observation of a local dSph Seg I the projected sensitivity to axion-photon coupling $g_{a\gamma\gamma}$ is, for axion masses below $m_a \lesssim 10^{-13} \text{ eV}$, expected to be orders of magnitudes better than for dedicated current and planned axion dark matter experiments, such as ADMX, HAYSTAC, etc. These parameter range is also allowed by the bounds obtained from CAST helioscope, SN 1987A constraints, and the CMB measurements. For higher values of m_a the SKA sensitivity weakens, because the axion-photon conversion probability in the regular magnetic field of a galaxy drops rapidly, if m_a is increased.

There are a number of uncertainties that enter the SKA projections, and whose effect we have estimated in the paper. The first issue is the dependence of radio flux on the value of the magnetic field in the dSph. The most conservative assumption is that the regular magnetic field is small, an order of magnitude smaller than expectations, and has negligible turbulent component, giving projections in Fig. 5 (right) and 6 (right). A turbulent magnetic field component, however, is expected to be large enough in dSph Seg I, such that the enhancement of the radio flux is expected, leading to results in Section 4.3. Finally, the axion density in the dSph is large enough that it can lead to significant Bose enhancement of the DM decay rates. To estimate the effect of such stimulated emission we used an iterative procedure that applies in the regime of a slowly varying axion density, in which

we obtained Bose enhancements of the DM decay rates of up to $\mathcal{O}(10^3)$. Unfortunately, most of the DM and axion parameter regime potentially relevant for SKA lies outside the validity of this approximation, and thus further work is needed. It is possible that the stimulated emission results in DM decays that are exponentially enhanced, such that in large regions of parameter space DM is unstable on cosmological timescales. Such runaway behavior is for instance obtained, if we use our iterative method outside its regime of validity. It is, however, also possible that a more fine grained time dependent simulation would result in quasistable solutions, similar to what we found with our iterative method when restricted to its regime of validity. While the issue of the effect of stimulated emission is not settled, it is useful to note that SKA can still probe regions of axion parameters for which our simulations are reliable, see Fig. 11, and further discussion in Section 4.4.

To conclude, searches for DM induced relativistic axion signals using radio telescopes can play an important role in axion physics, and can be complementary to other probes such as the axion haloscopes and helioscopes.

Acknowledgements

We thank Nick Rodd for useful discussions. The research of AK was supported by the National Research Foundation of Korea (NRF) funded by the Ministry of Education through the Center for Quantum Space Time (CQUeST) of Sogang University with Grant No. 2020R1A6A1A03047877 and by the Ministry of Science and ICT with grant number 2021R1F1A1057119. TK acknowledges support in the form of Junior Research Fellowship from the Council of Scientific & Industrial Research (CSIR), Government of India. SR acknowledges support from the APS-IUSSTF Professorship Award and the Department of Physics, University of Cincinnati for facilitating his visit to University of Cincinnati where this work was initiated. JZ acknowledges support in part by the DOE grant de-sc0011784 and NSF OAC-2103889. AK acknowledges the stay at School of Physical Sciences, Indian Association for the Cultivation of Science (IACS) where the initial part of this project was formulated.

Appendix A Iterative solutions for axion occupation number

In this appendix we give further details on finding the axion occupation number $\hat{f}_a(r)$ in (2.7) by iteratively solving for $n_a(r)$ in (2.6). We use two procedures, the *default* one, which was then used in the numerical analysis in the main text, and the *alternative* one, which is used as a consistency check. Both rely on the assumption that axion density is changing only slowly.

The default procedure. Since the change in n_a is slow compared to the time it takes for axions to traverse the dSph, we can solve Eq. (2.6) iteratively to find a quasi-equilibrium value of $n_a(r)$ at present. As a time step we use $\Delta t_{\text{dSph}} = R_{\text{dSph}}/c$, and assume that at $t = 0$ the initial axion number density in the dSph is zero, $n_a(t = 0) = 0$. The axion number density at time $t = (i + 1)\Delta t_{\text{dSph}}$ is then given by the l.h.s. of Eq. (2.6), where on the r.h.s.

the effective decay width is calculated with n_a from the i -th time step, $\Gamma_{\text{eff},i} = \Gamma_{\text{eff}}(n_{a,i})$,

$$n_{a,i+1}(r) = \int d\Omega \int_{\text{l.o.s.}} ds \frac{\Gamma_{\text{eff},i} N_a n_{\chi,i}}{4\pi}. \quad (\text{A.1})$$

In the calculation we also reduce appropriately the DM number density,

$$n_{\chi,i+1} = n_{\chi,i} \exp[-\Gamma_{\text{eff},i} \Delta t_{\text{dSph}}]. \quad (\text{A.2})$$

The results of this procedure for $m_\chi = 1 \mu\text{eV}$ and $\Gamma_\chi = 5.3 \cdot 10^{-38} \text{s}^{-1}$ are shown in Fig. 12, top left panel (green solid line). In this example, after about $15 \cdot 10^3$ iterations we reach the equilibrium value of n_a that corresponds to $\hat{f}_a \sim \mathcal{O}(10^3)$ in the inner part of dSph and $\hat{f}_a \sim \mathcal{O}(10)$ in the outskirts. The equilibrium value changes slowly with time since DM slowly decays, which results in decreasing equilibrium value of n_a . This change is very slow, however, since the effective DM decay time is still very long, $1/\Gamma_{\text{eff}} \gg t_U$. Note also, that the iteration step at which the equilibrium is reached, $i_{\text{itr}} \simeq 15 \cdot 10^3$, corresponds to a time of about $5 \cdot 10^7$ years, which is much less than the age of the dSph galaxy. The calculation of the equilibrium value of \hat{f}_a also agrees with the result obtained from the alternative iterative procedure (dashed green line in Fig. 12, top left panel), which we describe next.

The alternative procedure. To test that the assumption of a slowly varying axion number density is valid for a particular parameter region, we split the dSph into two halves, and use \hat{f}_a values from two different iterative steps, when calculating Γ_{eff} . That is, as in the default procedure we set in the 0-th step $n_{a,0} = 0$ and set the initial DM density to $n_{\chi,0} = n_{\text{DM}}$. To calculate the axion density at a given point \mathbf{p} , we then draw lines of sights from \mathbf{p} into all directions and divide the galaxy into two zones: (i) the near zone: $s < R_{\text{dSph}}$, and (ii) the far zone: $s > R_{\text{dSph}}$. Note that this division of dSph is different for different positions of \mathbf{p} . The n_a in the $(i+1)$ -th step is then calculated using

$$n_{a,i+1}(r) = \int d\Omega \int_{\text{l.o.s., near}} ds \frac{\Gamma_{\text{eff},i} N_a n_{\chi,i}}{4\pi} + \int d\Omega \int_{\text{l.o.s., far}} ds \frac{\Gamma_{\text{eff},i-1} N_a n_{\chi,i-1}}{4\pi}, \quad (\text{A.3})$$

while the change in DM density is given by

$$\delta n_{\chi,i+1} = -n_{\chi,i} \delta t \Gamma_{\text{eff},i}. \quad (\text{A.4})$$

The time step is taken to be $\delta t = \Delta t_{\text{dSph}}$ and $\Gamma_{\text{eff},i} = \Gamma_{\text{eff}}(n_{a,i})$. The motivation for using the split of dSph into near and far zones is that it takes time for axions to reach the point \mathbf{p} , and we thus use retarded values of n_a in the far zone. If the n_a changes slowly, the effect of retardation is negligible and one would obtain the same result for equilibrium value of n_a as in the default procedure, where the change in n_a for the whole dSph is treated as being instantaneous. In view of this interpretation we thus take n_a in the first step to be given by,

$$n_{a,1} = \int d\Omega \int_{\text{l.o.s., near}} ds \frac{\Gamma_{\text{eff},0} N_a n_{\chi,0}}{4\pi}, \quad (\text{A.5})$$

that is, we assume that the axions from the far zone have not yet reached point \mathbf{p} .

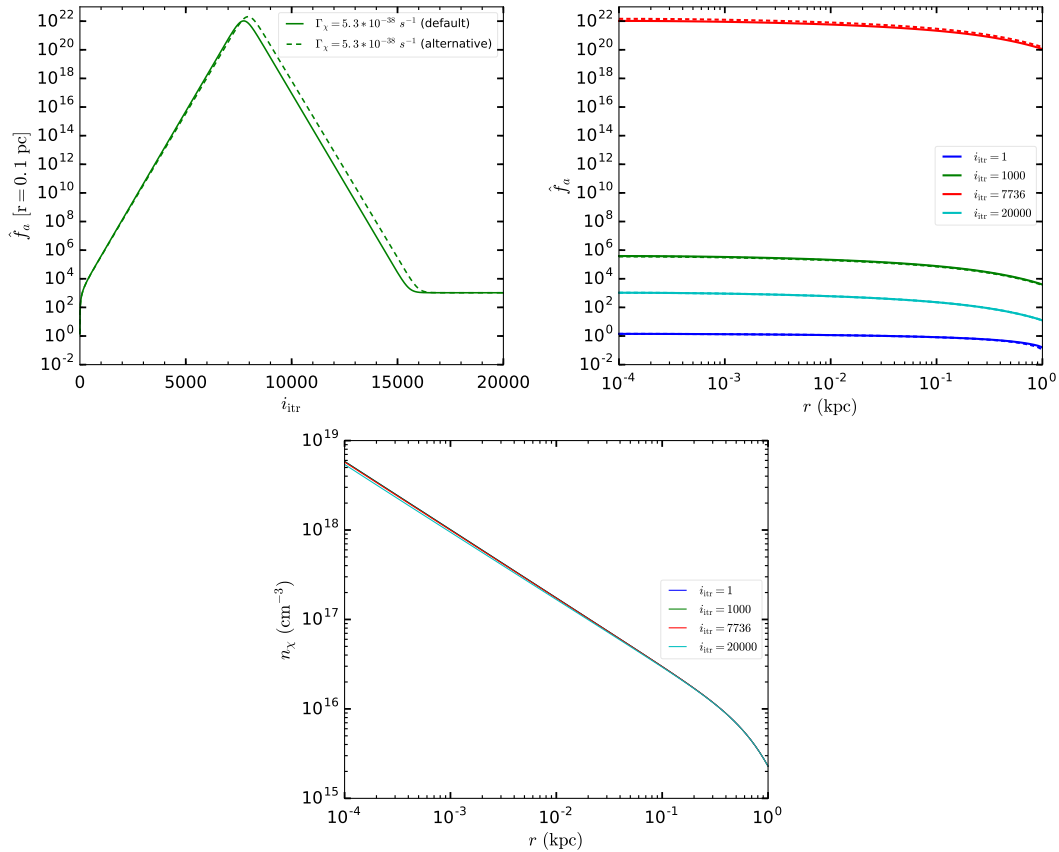


Figure 12. **Left top:** The variation of axion occupation number $\hat{f}_a(r = 0.1 \text{ pc})$ with iteration step, i_{itr} , in the default (solid green line) and alternative (dashed green line) methods, for $m_\chi = 1 \mu\text{eV}$ and $\Gamma_\chi = 5.3 \cdot 10^{-38} \text{ s}^{-1}$. **Right top:** Radial profile of the axion occupation number \hat{f}_a inside the dSph for four different iteration steps i_{itr} (step $i_{\text{itr}} = 7736$ represents the peak value for most r). **Bottom:** The corresponding changes in DM number density, n_χ .

The results for \hat{f}_a obtained from the alternative procedure for the $m_\chi = 1 \mu\text{eV}$, $\Gamma_\chi = 5.3 \cdot 10^{-38} \text{ s}^{-1}$ example are shown in Fig. 12, top left panel (green dashed line). Since in this case the change in n_a is slower than the propagation time in dSph the equilibrium values of n_a obtained with the default and alternative procedures agree.

References

- [1] J. E. Kim and G. Carosi, *Axions and the Strong CP Problem*, *Rev. Mod. Phys.* **82** (2010) 557–602, [[0807.3125](#)].
- [2] D. J. E. Marsh, *Axion Cosmology*, *Phys. Rept.* **643** (2016) 1–79, [[1510.07633](#)].
- [3] L. Di Luzio, M. Giannotti, E. Nardi and L. Visinelli, *The landscape of QCD axion models*, *Phys. Rept.* **870** (2020) 1–117, [[2003.01100](#)].
- [4] Z. G. Berezhiani, A. S. Sakharov and M. Y. Khlopov, *Primordial background of cosmological axions.*, *Soviet Journal of Nuclear Physics* **55** (July, 1992) 1063–1071.

- [5] J. Preskill, M. B. Wise and F. Wilczek, *Cosmology of the Invisible Axion*, *Phys. Lett. B* **120** (1983) 127–132.
- [6] L. F. Abbott and P. Sikivie, *A Cosmological Bound on the Invisible Axion*, *Phys. Lett. B* **120** (1983) 133–136.
- [7] M. Dine and W. Fischler, *The Not So Harmless Axion*, *Phys. Lett. B* **120** (1983) 137–141.
- [8] J. P. Conlon and M. C. D. Marsh, *The Cosmophenomenology of Axionic Dark Radiation*, *JHEP* **10** (2013) 214, [[1304.1804](#)].
- [9] M. C. D. Marsh, *Hints of a Cosmic Axion Background*, in *9th Patras Workshop on Axions, WIMPs and WISPs*, pp. 159–163, 2013, [DOI](#).
- [10] J. A. Dror, H. Murayama and N. L. Rodd, *Cosmic axion background*, *Phys. Rev. D* **103** (2021) 115004, [[2101.09287](#)].
- [11] K. Langhoff, N. J. Outmezguine and N. L. Rodd, *The Irreducible Axion Background*, [2209.06216](#).
- [12] J. L. Ouellet et al., *First Results from ABRACADABRA-10 cm: A Search for Sub- μeV Axion Dark Matter*, *Phys. Rev. Lett.* **122** (2019) 121802, [[1810.12257](#)].
- [13] J. L. Ouellet et al., *Design and implementation of the ABRACADABRA-10 cm axion dark matter search*, *Phys. Rev. D* **99** (2019) 052012, [[1901.10652](#)].
- [14] M. Silva-Feaver et al., *Design Overview of DM Radio Pathfinder Experiment*, *IEEE Trans. Appl. Supercond.* **27** (2017) 1400204, [[1610.09344](#)].
- [15] DMRADIO collaboration, L. Brouwer et al., *DMRadio- m^3 : A Search for the QCD Axion Below $1\ \mu\text{eV}$* , [2204.13781](#).
- [16] DMRADIO collaboration, L. Brouwer et al., *Proposal for a definitive search for GUT-scale QCD axions*, *Phys. Rev. D* **106** (2022) 112003, [[2203.11246](#)].
- [17] ADMX collaboration, S. J. Asztalos et al., *An Improved RF cavity search for halo axions*, *Phys. Rev. D* **69** (2004) 011101, [[astro-ph/0310042](#)].
- [18] ADMX collaboration, N. Du et al., *A Search for Invisible Axion Dark Matter with the Axion Dark Matter Experiment*, *Phys. Rev. Lett.* **120** (2018) 151301, [[1804.05750](#)].
- [19] ADMX collaboration, T. Braine et al., *Extended Search for the Invisible Axion with the Axion Dark Matter Experiment*, *Phys. Rev. Lett.* **124** (2020) 101303, [[1910.08638](#)].
- [20] B. M. Brubaker, L. Zhong, S. K. Lamoreaux, K. W. Lehnert and K. A. van Bibber, *Haystac axion search analysis procedure*, *Phys. Rev. D* **96** (Dec, 2017) 123008.
- [21] HAYSTAC collaboration, L. Zhong et al., *Results from phase 1 of the HAYSTAC microwave cavity axion experiment*, *Phys. Rev. D* **97** (2018) 092001, [[1803.03690](#)].
- [22] C. M. Adair et al., *Search for Dark Matter Axions with CAST-CAPP*, *Nature Commun.* **13** (2022) 6180, [[2211.02902](#)].
- [23] MADMAX WORKING GROUP collaboration, A. Caldwell, G. Dvali, B. Majorovits, A. Millar, G. Raffelt, J. Redondo et al., *Dielectric Haloscopes: A New Way to Detect Axion Dark Matter*, *Phys. Rev. Lett.* **118** (2017) 091801, [[1611.05865](#)].
- [24] A. J. Millar, G. G. Raffelt, J. Redondo and F. D. Steffen, *Dielectric Haloscopes to Search for Axion Dark Matter: Theoretical Foundations*, *JCAP* **01** (2017) 061, [[1612.07057](#)].

- [25] PLANCK collaboration, N. Aghanim et al., *Planck 2018 results. VI. Cosmological parameters*, *Astron. Astrophys.* **641** (2020) A6, [[1807.06209](#)].
- [26] D. Baumann, D. Green and B. Wallisch, *New Target for Cosmic Axion Searches*, *Phys. Rev. Lett.* **117** (2016) 171301, [[1604.08614](#)].
- [27] J. Eby, S. Shirai, Y. V. Stadnik and V. Takhistov, *Probing relativistic axions from transient astrophysical sources*, *Phys. Lett. B* **825** (2022) 136858, [[2106.14893](#)].
- [28] J. P. Conlon and M. C. D. Marsh, *Excess Astrophysical Photons from a 0.1–1 keV Cosmic Axion Background*, *Phys. Rev. Lett.* **111** (2013) 151301, [[1305.3603](#)].
- [29] T. Moroi, K. Nakayama and Y. Tang, *Axion-photon conversion and effects on 21 cm observation*, *Phys. Lett. B* **783** (2018) 301–305, [[1804.10378](#)].
- [30] T. Higaki, K. Nakayama and F. Takahashi, *Cosmological constraints on axionic dark radiation from axion-photon conversion in the early Universe*, *JCAP* **09** (2013) 030, [[1306.6518](#)].
- [31] J. Jaeckel and W. Yin, *Shining ALP dark radiation*, *Phys. Rev. D* **105** (2022) 115003, [[2110.03692](#)].
- [32] J. Jaeckel and W. Yin, *Using the spectrum of dark radiation as a probe of reheating*, *Phys. Rev. D* **103** (2021) 115019, [[2102.00006](#)].
- [33] F. Schiavone, D. Montanino, A. Mirizzi and F. Capozzi, *Axion-like particles from primordial black holes shining through the Universe*, *JCAP* **08** (2021) 063, [[2107.03420](#)].
- [34] Y. Cui, M. Pospelov and J. Pradler, *Signatures of Dark Radiation in Neutrino and Dark Matter Detectors*, *Phys. Rev. D* **97** (2018) 103004, [[1711.04531](#)].
- [35] Y. Gu, L. Wu and B. Zhu, *Axion dark radiation: Hubble tension and the Hyper-Kamiokande neutrino experiment*, *Phys. Rev. D* **105** (2022) 095008, [[2105.07232](#)].
- [36] R. Braun, T. L. Bourke, J. A. Green, E. Keane and J. Wagg, *Advancing Astrophysics with the Square Kilometre Array*, *PoS AASKA14* (2015) 174.
- [37] R. Braun et al. https://www.skao.int/sites/default/files/documents/d2-SKA-TEL-SKO-0000818-01_SKA1_Science_Perform.pdf, 2017.
- [38] K. Kelley and P. J. Quinn, *A Radio Astronomy Search for Cold Dark Matter Axions*, *Astrophys. J. Lett.* **845** (2017) L4, [[1708.01399](#)].
- [39] G. Sigl, *Astrophysical Haloscopes*, *Phys. Rev. D* **96** (2017) 103014, [[1708.08908](#)].
- [40] A. Caputo, C. P. n. Garay and S. J. Witte, *Looking for Axion Dark Matter in Dwarf Spheroidals*, *Phys. Rev. D* **98** (2018) 083024, [[1805.08780](#)].
- [41] R. A. Battye, B. Garbrecht, J. I. McDonald, F. Pace and S. Srinivasan, *Dark matter axion detection in the radio/mm-waveband*, *Phys. Rev. D* **102** (2020) 023504, [[1910.11907](#)].
- [42] J.-W. Wang, X.-J. Bi and P.-F. Yin, *Detecting axion dark matter through the radio signal from Omega Centauri*, *Phys. Rev. D* **104** (2021) 103015, [[2109.00877](#)].
- [43] A. Ayad and G. Beck, *Axion-like particle searches with MeerKAT and SKA*, *JCAP* **03** (2022) 005, [[2010.05773](#)].
- [44] CAST collaboration, V. Anastassopoulos et al., *New CAST Limit on the Axion-Photon Interaction*, *Nature Phys.* **13** (2017) 584–590, [[1705.02290](#)].

- [45] A. Payez, C. Evoli, T. Fischer, M. Giannotti, A. Mirizzi and A. Ringwald, *Revisiting the SN1987A gamma-ray limit on ultralight axion-like particles*, *JCAP* **02** (2015) 006, [[1410.3747](#)].
- [46] A. Mirizzi, J. Redondo and G. Sigl, *Constraining resonant photon-axion conversions in the Early Universe*, *JCAP* **08** (2009) 001, [[0905.4865](#)].
- [47] M. Cicoli, J. P. Conlon, M. C. D. Marsh and M. Rummel, *3.55 keV photon line and its morphology from a 3.55 keV axionlike particle line*, *Phys. Rev. D* **90** (2014) 023540, [[1403.2370](#)].
- [48] M. Geha, B. Willman, J. D. Simon, L. E. Strigari, E. N. Kirby, D. R. Law et al., *The Least Luminous Galaxy: Spectroscopy of the Milky Way Satellite Segue 1*, *Astrophys. J.* **692** (2009) 1464–1475, [[0809.2781](#)].
- [49] J. D. Simon, M. Geha, Q. E. Minor, G. D. Martinez, E. N. Kirby, J. S. Bullock et al., *A COMPLETE SPECTROSCOPIC SURVEY OF THE MILKY WAY SATELLITE SEGUE 1: THE DARKEST GALAXY*, *The Astrophysical Journal* **733** (may, 2011) 46.
- [50] X. Calmet and F. Kuipers, *Bounds on very weakly interacting ultra light scalar and pseudoscalar dark matter from quantum gravity*, *Eur. Phys. J. C* **80** (2020) 781, [[2008.06243](#)].
- [51] DES collaboration, A. Chen et al., *Constraints on dark matter to dark radiation conversion in the late universe with DES-Y1 and external data*, *Phys. Rev. D* **103** (2021) 123528, [[2011.04606](#)].
- [52] T. Bringmann, F. Kahlhoefer, K. Schmidt-Hoberg and P. Walia, *Converting nonrelativistic dark matter to radiation*, *Phys. Rev. D* **98** (2018) 023543, [[1803.03644](#)].
- [53] A. Geringer-Sameth, S. M. Koushiappas and M. Walker, *Dwarf galaxy annihilation and decay emission profiles for dark matter experiments*, *Astrophys. J.* **801** (2015) 74, [[1408.0002](#)].
- [54] A. Caputo, M. Regis, M. Taoso and S. J. Witte, *Detecting the Stimulated Decay of Axions at RadioFrequencies*, *JCAP* **03** (2019) 027, [[1811.08436](#)].
- [55] G. Alonso-Álvarez, R. S. Gupta, J. Jaeckel and M. Spannowsky, *On the Wondrous Stability of ALP Dark Matter*, *JCAP* **03** (2020) 052, [[1911.07885](#)].
- [56] G. Raffelt and L. Stodolsky, *Mixing of the Photon with Low Mass Particles*, *Phys. Rev. D* **37** (1988) 1237.
- [57] Y. Grossman, S. Roy and J. Zupan, *Effects of initial axion production and photon axion oscillation on type Ia supernova dimming*, *Phys. Lett. B* **543** (2002) 23–28, [[hep-ph/0204216](#)].
- [58] P. Carenza, C. Evoli, M. Giannotti, A. Mirizzi and D. Montanino, *Turbulent axion-photon conversions in the Milky Way*, *Phys. Rev. D* **104** (2021) 023003, [[2104.13935](#)].
- [59] S. Colafrancesco, S. Profumo and P. Ullio, *Detecting dark matter WIMPs in the Draco dwarf: A multi-wavelength perspective*, *Phys. Rev. D* **75** (2007) 023513, [[astro-ph/0607073](#)].
- [60] A. McDaniel, T. Jeltema, S. Profumo and E. Storm, *Multiwavelength Analysis of Dark Matter Annihilation and RX-DMFIT*, *JCAP* **09** (2017) 027, [[1705.09384](#)].
- [61] A. Natarajan, J. E. Aguirre, K. Spekkens and B. S. Mason, *Green Bank Telescope Constraints on Dark Matter Annihilation in Segue I*, [1507.03589](#).

- [62] T. G. Arshakian, R. Beck, M. Krause and D. Sokoloff, *Evolution of magnetic fields in galaxies and future observational tests with the Square Kilometre Array*, *Astron. Astrophys.* **494** (2009) 21, [[0810.3114](#)].
- [63] M. Regis, L. Richter, S. Colafrancesco, S. Profumo, W. J. G. de Blok and M. Massardi, *Local Group dSph radio survey with ATCA – II. Non-thermal diffuse emission*, *Mon. Not. Roy. Astron. Soc.* **448** (2015) 3747–3765, [[1407.5482](#)].
- [64] A. R. Taylor, *The Square Kilometre Array*, in *A Giant Step: from Milli- to Micro-arcsecond Astrometry* (W. J. Jin, I. Platais and M. A. C. Perryman, eds.), vol. 248, pp. 164–169, July, 2008, [DOI](#).
- [65] J. D. Bregman, *System Design and Wide-field Imaging Aspects of Synthesis Arrays with Phased Array Stations*, Ph.D. thesis, University of Groningen, Netherlands, Dec., 2012.
- [66] J. G. Bij de Vaate, D. I. L. de Villiers, D. B. Davidson and W. A. van Cappellen, *Expanding the field of view: station design for the AAMID SKA radio telescope*, *Experimental Astronomy* **51** (Feb., 2021) 1–16.
- [67] Z. Chen, Y.-L. S. Tsai and Q. Yuan, *Sensitivity of SKA to dark matter induced radio emission*, *JCAP* **09** (2021) 025, [[2105.00776](#)].
- [68] <https://science.nrao.edu/facilities/vla/docs/manuals/obsguide/modes/mosaicking>.
- [69] T. J. Cornwell, *Radio-interferometric imaging of very large objects.*, *A&A* **202** (Aug., 1988) 316–321.
- [70] R. Ghara, T. R. Choudhury and K. K. Datta, *21-cm signature of the first sources in the Universe: Prospects of detection with SKA*, *Mon. Not. Roy. Astron. Soc.* **460** (2016) 827–843, [[1511.07448](#)].
- [71] A. Kar, S. Mitra, B. Mukhopadhyaya and T. R. Choudhury, *Heavy dark matter particle annihilation in dwarf spheroidal galaxies: radio signals at the SKA telescope*, *Phys. Rev. D* **101** (2020) 023015, [[1905.11426](#)].
- [72] PLANCK collaboration, P. A. R. Ade et al., *Planck 2015 results. XIX. Constraints on primordial magnetic fields*, *Astron. Astrophys.* **594** (2016) A19, [[1502.01594](#)].
- [73] R. Beck, *Magnetic fields in galaxies*, in *Space Sciences Series of ISSI*, pp. 215–230. Springer New York, 2011. [DOI](#).
- [74] M. Kachelriess and J. Tjemsland, *On the origin and the detection of characteristic axion wiggles in photon spectra*, *JCAP* **01** (2022) 025, [[2111.08303](#)].
- [75] J. P. Conlon and F. V. Day, *3.55 keV photon lines from axion to photon conversion in the Milky Way and M31*, *JCAP* **11** (2014) 033, [[1404.7741](#)].